of the measured dip in the normalized homodyne signal is equal to that of the coupling-induced transmission window $\Gamma_{OMIT} \approx \Gamma_m (1 + C)$, where $C \equiv \Omega_c^2/\Gamma_m\kappa$ is an equivalent optomechanical cooperativity parameter (*14*). From the model (Eq. 5), the expected probe transmission on resonance is simply given by $t_p'(\Delta' = 0) = C/(C + 1)$. Our data match these expectations well if we allow for a linear correction factor in the optomechanical coupling frequency Ω_c due to modal coupling (SOM Sec. 7) and losses in the fiber taper. We have reached probe power transmission $|t_p'|^2$ up to 81%, indicating the high contrast achievable in OMIT.

In fact, any optomechanical system reaching $C \gtrsim 1$ can realize an appreciable control-induced probe transmission, as desired, for example, in all-optical switches. Interestingly, the systems currently available reach $C \approx 1$ with only thousands (*26*) or even hundreds (*27*) of control photons in the cavity, and recently emerging integrated nano-optomechanical structures (*28*) may be able to further reduce this number. The resulting extreme optical nonlinearities could be of interest for both fundamental and applied studies.

The tunable probe transmission window also modifies the propagation of a probe pulse due to the variation of the complex phase picked by its different frequency components. Indeed, a resonant probe pulse experiences a group delay of $\tau_g \approx 2/\Gamma_{OMIT}$ in the regime $C \gtrsim 1$ of interest (SOM Sec. 6), a value exceeding several seconds in some available optomechanical systems (*29*). However, undistorted pulse propagation only occurs if the full probe-pulse spectrum is contained within the transparency window of the system. This restricts the effectiveness of such a delay due to the fixed delay-bandwidth product of $\tau_g \Gamma_{OMIT} \approx 2$. A cascade of systems may alleviate this shortcoming—the most interesting scenario being a large array of concatenated optomechanical systems, as suggested in the context of OMIT (*16*, *17*, *30*), and radio frequency/microwave photonics (*15*). The group delay could then be dynamically tuned while the probe pulse is propagating through the array. Such systems could be practically implemented in lithographically designed optomechanical systems both in the microwave (*27*) and optical (*31*) domain.

Note added in proof: After online publication of this work, OMIT has also been reported in microwave optomechanical systems by Teufel *et al*. (*32*).

References and Notes

1. M. Fleischhauer, A. Imamoglu, J. P. Marangos, *Rev. Mod. Phys.* **77**, 633 (2005).
2. K.-J. Boller, A. Imamoglu, S. E. Harris, *Phys. Rev. Lett.* **66**, 2593 (1991).
3. A. Kasapi, M. Jain, G. Y. Yin, S. E. Harris, *Phys. Rev. Lett.* **74**, 2447 (1995).
4. L. V. Hau, S. E. Harris, Z. Dutton, C. H. Behroozi, *Nature* **397**, 594 (1999).
5. D. F. Phillips, A. Fleischhauer, A. Mair, R. L. Walsworth, M. D. Lukin, *Phys. Rev. Lett.* **86**, 783 (2001).
6. C. Liu, Z. Dutton, C. H. Behroozi, L. V. Hau, *Nature* **409**, 490 (2001).
7. M. D. Lukin, A. Imamoglu, *Nature* **413**, 273 (2001).
8. A. V. Turukhin *et al*., *Phys. Rev. Lett.* **88**, 023602 (2002).
9. D. Brunner *et al*., *Science* **325**, 70 (2009).
10. T. J. Kippenberg, H. Rokhsari, T. Carmon, A. Scherer, K. J. Vahala, *Phys. Rev. Lett.* **95**, 033901 (2005).
11. A. Schliesser, P. Del'Haye, N. Nooshi, K. J. Vahala, T. J. Kippenberg, *Phys. Rev. Lett.* **97**, 243905 (2006).
12. O. Arcizet, P.-F. Cohadon, T. Briant, M. Pinard, A. Heidmann, *Nature* **444**, 71 (2006).
13. S. Gigan *et al*., *Nature* **444**, 67 (2006).
14. S. Gröblacher, K. Hammerer, M. R. Vanner, M. Aspelmeyer, *Nature* **460**, 724 (2009).
15. Q. Lin *et al*., *Nat. Photonics* **4**, 236 (2010).
16. A. Schliesser, Cavity optomechanics and optical frequency comb generation with silica whispering-gallery-mode microresonators, Thesis, Ludwig-Maximilians-Universität München (2009); http://edoc.ub.uni-muenchen.de/10940.
17. A. Schliesser, T. J. Kippenberg, in *Advances in Atomic, Molecular and Optical Physics*, Vol. 58, E. Arimondo, P. Berman, C. C. Lin, Eds. (Elsevier Academic Press, 2010), pp. 207–323.
18. G. S. Agarwal, S. Huang, *Phys. Rev. A* **81**, 041803 (2010).
19. J. Zhang, K. Peng, S. L. Braunstein, *Phys. Rev. A* **68**, 013808 (2003).
20. M. Mücke *et al*., *Nature* **465**, 755 (2010).
21. C. Fabre *et al*., *Phys. Rev. A* **49**, 1337 (1994).
22. F. Marquardt, J. P. Chen, A. A. Clerk, S. M. Girvin, *Phys. Rev. Lett.* **99**, 093902 (2007).
23. J. M. Dobrindt, I. Wilson-Rae, T. J. Kippenberg, *Phys. Rev. Lett.* **101**, 263602 (2008).
24. M. Cai, O. Painter, K. J. Vahala, *Phys. Rev. Lett.* **85**, 74 (2000).
25. A. Schliesser, O. Arcizet, R. Rivière, G. Anetsberger, T. Kippenberg, *Nat. Phys.* **5**, 509 (2009).
26. G. Anetsberger *et al*., *Nat. Phys.* **5**, 909 (2009).
27. C. A. Regal, J. D. Teufel, K. W. Lehnert, *Nat. Phys.* **4**, 555 (2008).
28. M. Eichenfield, R. Camacho, J. Chan, K. J. Vahala, O. Painter, *Nature* **459**, 550 (2009).
29. J. D. Thompson *et al*., *Nature* **452**, 72 (2008).
30. D. E. Chang, A. H. Safavi-Naeini, M. Hafezi, O. Painter, http://arxiv.org/abs/1006.3829 (2010).
31. M. Eichenfield, J. Chan, R. M. Camacho, K. J. Vahala, O. Painter, *Nature* **462**, 78 (2009).
32. J. D. Teufel *et al*.; http://arxiv.org/abs/1011.3067 (2010).

33. T.J.K. acknowledges financial support by the Max Planck Society, European Research Council Starting Grant (SiMP), the European Union's MINOS, a Marie Curie Excellence Grant, the Swiss National Science Foundation, National Centre of Competence and Research of Quantum Photonics, and the Defense Advanced Research Projects Agency. S.D. is funded by a Marie Curie Individual Fellowship.

Supporting Online Material

www.sciencemag.org/cgi/content/full/science.1195596/DC1
SOM Text
Figs. S1 to S3
References

26 July 2010; accepted 1 November 2010
Published online 11 November 2010;
10.1126/science.1195596

A Determination of the Cloud Feedback from Climate Variations over the Past Decade

A. E. Dessler

Estimates of Earth's climate sensitivity are uncertain, largely because of uncertainty in the long-term cloud feedback. I estimated the magnitude of the cloud feedback in response to short-term climate variations by analyzing the top-of-atmosphere radiation budget from March 2000 to February 2010. Over this period, the short-term cloud feedback had a magnitude of 0.54 ± 0.74 (2σ) watts per square meter per kelvin, meaning that it is likely positive. A small negative feedback is possible, but one large enough to cancel the climate's positive feedbacks is not supported by these observations. Both long- and short-wave components of short-term cloud feedback are also likely positive. Calculations of short-term cloud feedback in climate models yield a similar feedback. I find no correlation in the models between the short- and long-term cloud feedbacks.

Much of the global warming expected over the next century comes from feedbacks rather than direct warming from CO_2 and other greenhouse agents. Of these feedbacks, the most complex and least understood is the cloud feedback (*1*, *2*). Clouds affect the climate by reflecting incoming solar radiation back to space, which tends to cool the climate, and by trapping outgoing infrared radiation, which tends to warm the climate. In our present climate, the reflection of solar energy back to space dominates, and the net effect of clouds is to reduce the net flux of incoming energy at the top of the atmosphere (TOA) by ~20 W/m^2, as compared to an otherwise identical planet without clouds. The cloud feedback refers to changes in this net effect of clouds as the planet warms. If, as the climate warms, cloud changes further reduce net incoming energy, this will offset some of the warming, resulting in a negative cloud feedback. If, on the other hand, cloud changes lead to increases in net incoming energy, then the change will amplify the initial warming, resulting in a positive cloud feedback.

Climate models disagree on the magnitude of the cloud feedback, simulating a range of cloud feedbacks in response to long-term global warming from near zero to a positive feedback of 1 W/m^2/K (*3*, *4*). This spread is the single most important reason for the large spread in the climate

Department of Atmospheric Sciences, Texas A&M University, College Station, TX, USA. E-mail: adessler@tamu.edu

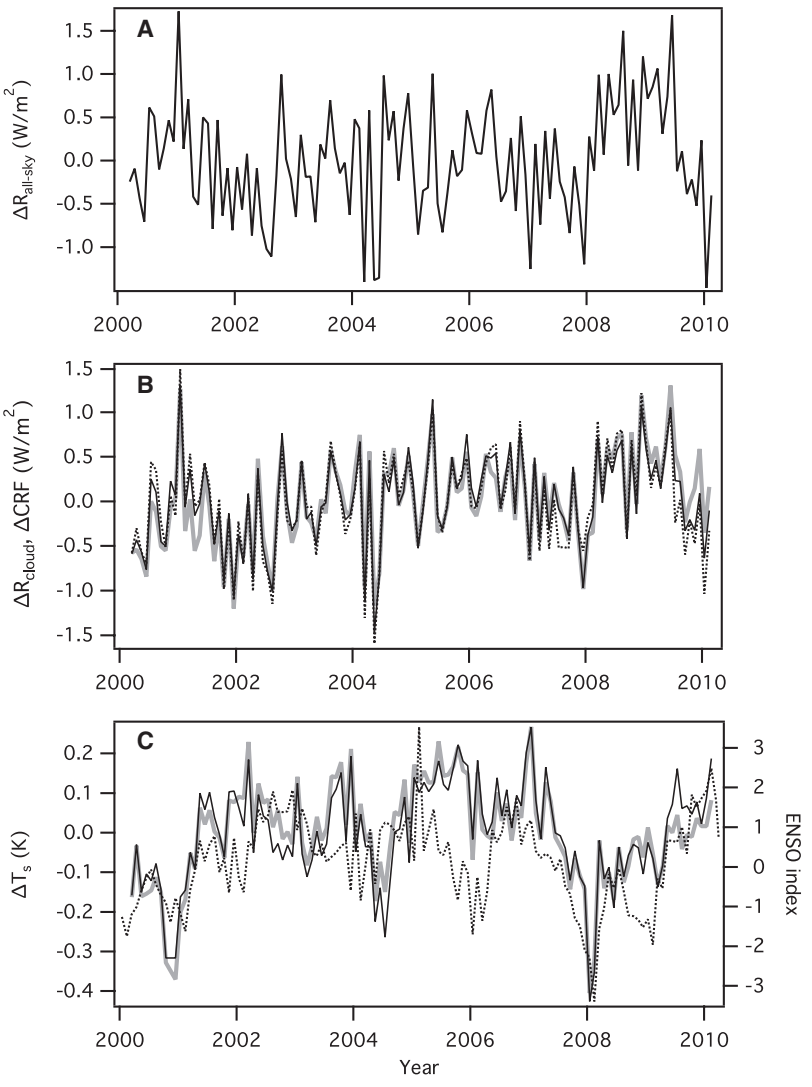

Fig. 1. (**A**) Global and monthly averaged $\Delta R_{all\text{-}sky}$, measured by CERES. (**B**) Global and monthly averaged ΔR_{cloud} calculated from CERES measurements and reanalyses (solid lines) and ΔCRF (dotted line) from the CERES and ECMWF interim reanalysis. (**C**) Global and monthly averaged ΔT_s from reanalyses (solid lines), along with an ENSO index (*23*) (dotted line). In (B) and (C), calculations using CERES data with the ECMWF interim reanalysis and MERRA are the solid black and gray lines, respectively. The sign convention used in this paper is that downward fluxes are positive.

sensitivities among climate models (*5*, *6*). Despite the importance of the cloud feedback, there have been few estimates of its magnitude from observations. Previous work has generally focused on just part of the problem [for example, the tropics (*7*, *8*) or low clouds (*9*)], and these analyses differ even on the sign of the cloud feedback.

In this paper, I present an estimate of the global cloud feedback in response to short-term climate fluctuations over the past decade and compare these results to those from climate models. The primary source of climate variations over this time period is the El Niño–Southern Oscillation (ENSO), which is a self-sustained coupled atmosphere-ocean mode of variability (*10*). During the El Niño phase, monthly and global-average surface temperature are several tenths of a degree Celsius warmer than during the La Niña phase, and these climate variations have previously been used to quantify the water vapor feedback (*11*, *12*).

Figure 1A shows a time series of monthly and global-average anomalies of TOA net flux ($\Delta R_{all\text{-}sky}$) between March 2000 and February 2010 measured by the Clouds and the Earth's Radiant Energy System (CERES) (*13*) instruments onboard NASA's Terra satellite. This time series (*14*) is stable to better than 0.5 W/m^2/decade [the stability of the short-wave component is 0.3 W/m^2/decade (*15*) and that of the long-wave component is 0.2 W/m^2/decade, from comparisons to Atmospheric Infrared Sounder measurements].

Table 1. Cloud feedback values. All uncertainties are 2σ. Feedbacks are calculated from a 100-year segment of a control run, except for CCSM3, which is based on 80 years. N/A, not available.

Model	Short-term cloud feedback			Long-term cloud feedback*	Equilibrium climate sensitivity†
	Total	Long-wave component	Short-wave component		
NCAR PCM1	1.11 ± 0.20	0.52 ± 0.11	0.60 ± 0.21	0.18	2.1
IPSL-CM4	1.05 ± 0.16	1.17 ± 0.13	–0.12 ± 0.14	1.06	4.4
INM-CM3.0	0.98 ± 0.18	0.77 ± 0.10	0.21 ± 0.19	0.35	2.1
UKMO-HadCM3	0.88 ± 0.31	0.57 ± 0.15	0.31 ± 0.35	1.08	3.3
ECHAM/MPI-OM	0.74 ± 0.20	0.97 ± 0.09	–0.23 ± 0.20	1.18	3.4
NCAR CCSM3	0.62 ± 0.26	0.17 ± 0.12	0.45 ± 0.25	0.14	2.7
GFDL-CM2.0	0.41 ± 0.22	–0.03 ± 0.11	0.43 ± 0.26	0.67	2.9
GFDL-CM2.1	0.34 ± 0.20	0.40 ± 0.08	–0.06 ± 0.23	0.81	3.4
ECMWF-CERES	0.54 ± 0.74	0.43 ± 0.45	0.12 ± 0.78	N/A	N/A
MERRA-CERES	0.46 ± 0.77	0.27 ± 0.47	0.19 ± 0.76	N/A	N/A

*From table 1 of Soden and Held (*3*). †Equilibrium climate change (in degrees kelvin) in response to a doubling of CO_2 [from table 8.2 of Randall *et al.* (*1*)].

From these data, I extracted the part of $\Delta R_{all\text{-}sky}$ caused by changing clouds, hereafter referred to as ΔR_{cloud}. To do this, I took cloud radiative-forcing anomalies (ΔCRF) and adjusted those to account for the impact of changing tem-

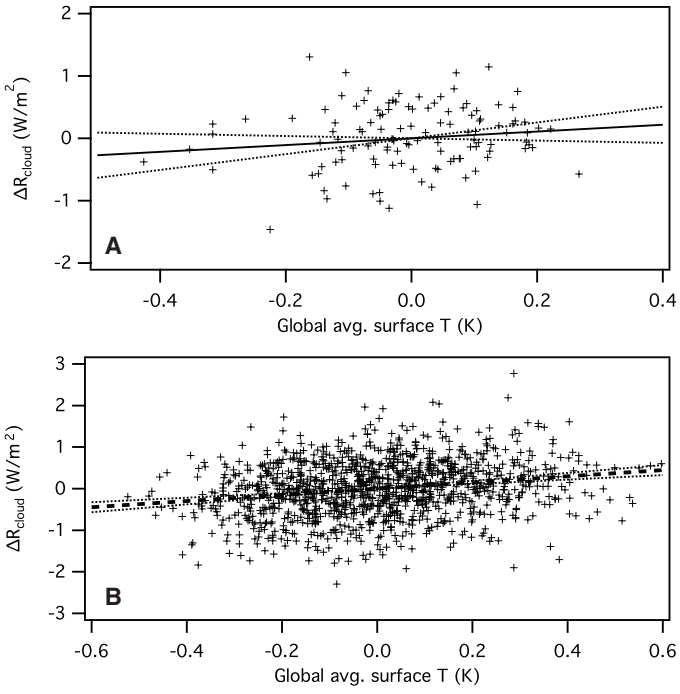

Fig. 2. (**A**) Scatter plot of monthly average values of ΔR_{cloud} versus ΔT_s using CERES and ECMWF interim data. (**B**) Scatter plot of monthly averages of the same quantities from 100 years of a control run of the ECHAM/MPI-OM model. In all plots, the solid line is a linear least-squares fit and the dotted lines are the 2σ confidence interval of the fit.

perature, water vapor, surface albedo, and radiative forcing, ultimately yielding ΔR_{cloud} (*16*, *17*). ΔCRF is the change in TOA net flux anomaly if clouds were instantaneously removed, with everything else held fixed, and it is determined by subtracting $\Delta R_{all\text{-}sky}$, obtained from CERES measurements, from the clear-sky flux anomalies $\Delta R_{clear\text{-}sky}$, obtained from a reanalysis system. The ΔCRF time series is plotted in Fig. 1B.

In a reanalysis system, conventional and satellite-based meteorological observations are combined within a weather forecast assimilation system in order to produce a global and physically consistent picture of the state of the atmosphere. I used both the ECMWF (European Centre for Medium-Range Weather Forecasts) interim reanalysis (*18*) and NASA's Modern Era Retrospective analysis for Research and Applications (MERRA) (*19*) in the calculations. The fields being used here (mainly water vapor and temperature) are constrained in the reanalysis by high-density satellite measurements. Previous work has shown that $\Delta R_{clear\text{-}sky}$ can be calculated accurately given water vapor and temperature distributions (*20*, *21*). And, given suggestions of biases in measured clear-sky fluxes (*22*), I chose to use the reanalysis fluxes here.

The water vapor, temperature, and surface albedo anomalies used to convert ΔCRF into ΔR_{cloud} also come from the reanalyses. Additionally, the all-sky radiative forcing change caused primarily by changes in long-lived greenhouse gases over the March 2000–February 2010 period is estimated to be +0.25 W/m^2. Following Soden *et al*. (*16*), I multiply the all-sky radiative forcing by 0.16 to estimate the difference between clear-sky and all-sky radiative forcing. Anomalies of all quantities are calculated by subtracting from each month's value the average for that month over the entire time series. Figure 1B shows time series of ΔR_{cloud}, and it shows that the differences between ΔCRF and ΔR_{cloud} are small for these data. For compactness, I will refer to the calculated values of ΔR_{cloud} as "the observations."

Figure 1C shows the accompanying time series of global-average and monthly mean surface temperature anomalies (ΔT_s) from the reanalyses. Also plotted is an ENSO index (*23*), and the close association between that and ΔT_s verifies that ENSO is the primary source of variations in ΔT_s.

The cloud feedback is conventionally defined as the change in ΔR_{cloud} per unit of change in ΔT_s. Figure 2A is a scatter plot of monthly values of ΔR_{cloud} versus ΔT_s, calculated using ECMWF interim meteorological fields. The slope of this scatter plot is the strength of the cloud feedback, and it is estimated by a traditional least-squares fit to be 0.54 ± 0.72 (2σ) W/m^2/K (the slope using the MERRA is 0.46 ± 0.75 W/m^2/K). Because I have defined downward flux as positive, the positive slope here means that, as the surface warms, clouds trap additional energy; in other words, the cloud feedback here is positive.

The uncertainty quoted above is the statistical uncertainty of the fit. The impact of a spurious long-term trend in either $\Delta R_{all\text{-}sky}$ or $\Delta R_{clear\text{-}sky}$ is estimated by adding in a trend of ±0.5 W/m^2/decade into the CERES data. This changes the calculated feedback by ±0.18 W/m^2/K. Adding these errors in quadrature yields a total uncertainty of 0.74 and 0.77 W/m^2/K in the calculations, using the ECMWF and MERRA reanalyses, respectively. Other sources of uncertainty are negligible.

Given the uncertainty, the possibility of a small negative feedback cannot be excluded. There have been inferences (*7*, *8*) of a large negative cloud feedback in response to short-term climate variations that can substantially cancel the other feedbacks operating in our climate system. This would require the cloud feedback to be in the range of –1.0 to –1.5 W/m^2/K or larger, and I see no evidence to support such a large negative cloud feedback [these inferences of large negative feedbacks have also been criticized on methodological grounds (*24*, *25*)].

I have not explicitly considered the direct effect of aerosols on TOA flux in this analysis. The effects of aerosols are obviously included in the $\Delta R_{all\text{-}sky}$ measurements, but the $\Delta R_{clear\text{-}sky}$ calculations include only an annual-cycle climatology. As a result, the radiative impact of interannual variations in aerosols will be included in ΔR_{cloud}. But aerosols' radiative impact is not expected to correlate with ΔT_s, so the effect of aerosols is to add uncertainty to the cloud feedback calculation but should not introduce a bias.

This definition of the cloud feedback is a standard approach for quantifying feedbacks (*26*). It only requires an association between T_s and ΔR_{cloud} but does not imply any specific physical mechanism connecting them. The recent suggestion that feedback analyses suffer from a cause-and-effect problem (*27*) does not apply here: The climate variations being analyzed here are primarily driven by ENSO, and there has been no suggestion that ENSO is caused by cloud variations (*10*).

Obviously, the correlation between ΔR_{cloud} and ΔT_s is weak (r^2 = 2%), meaning that factors other than T_s are important in regulating ΔR_{cloud}. An example is the Madden-Julian Oscillation (*7*), which has a strong impact on ΔR_{cloud} but no effect on ΔT_s. This does not mean that ΔT_s exerts no control on ΔR_{cloud}, but rather that the influence is hard to quantify because of the influence of other factors. As a result, it may require several more decades of data to significantly reduce the uncertainty in the inferred relationship.

In this way, the cloud feedback is quite different from the water vapor feedback. The water vapor feedback is primarily controlled by tropical upper-tropospheric water vapor (*28*), which in turn is strongly controlled by tropical surface temperatures (*11*, *29*). Because of this, the relationship between surface temperature and the radiative impact of water vapor is tight and completely clear in just a few years of data. This is one of the main reasons why our confidence in the water vapor feedback is so strong (*30*).

One obvious question is whether climate models also reproduce this cloud feedback in response to short-term climate variations. To test this, I analyzed control runs from fully coupled climate models, in which atmospheric greenhouse gas abundances and other forcings are held constant at either their preindustrial or present-day concentrations; thus, there are no long-term trends in the models' climate, and the climate variations in the model runs are entirely due to internal variability. The control runs were obtained from the World Climate Research Programme's (WCRP's) Coupled Model Intercomparison Project phase 3 (CMIP3) multimodel data set (*31*).

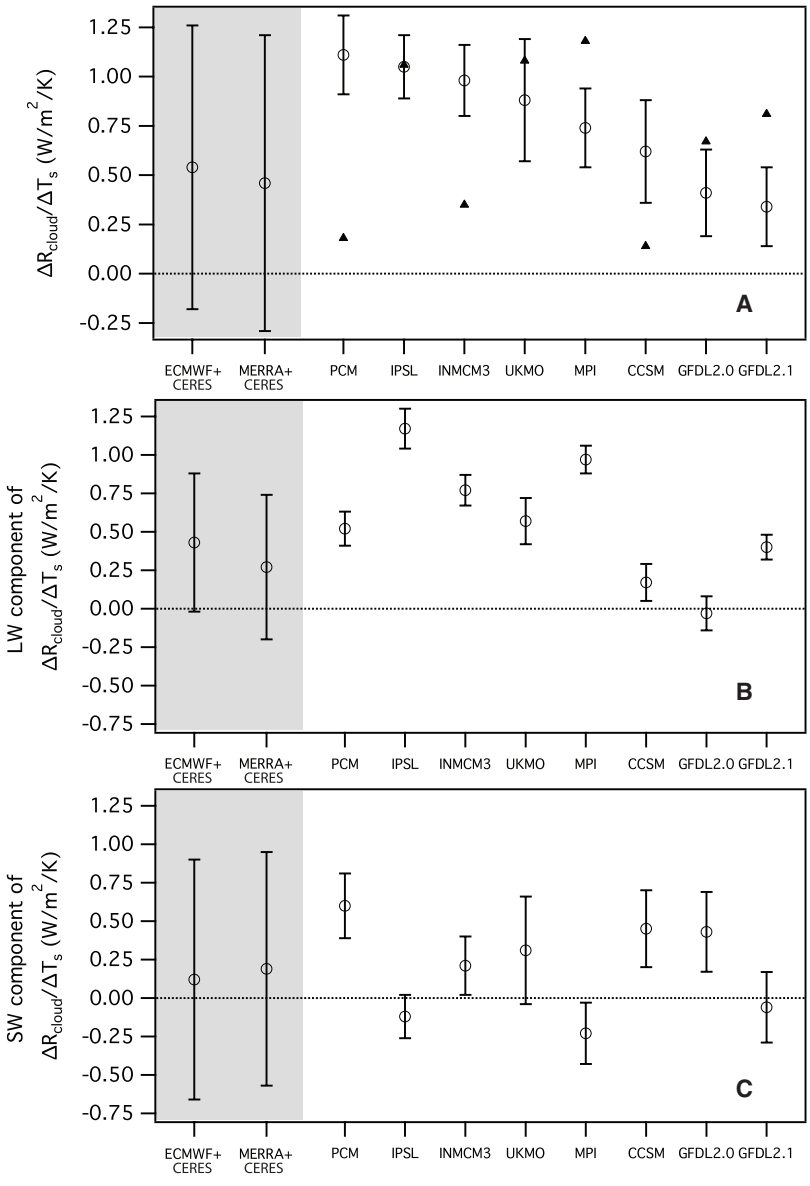

Fig. 3. (**A**) Comparison of the total cloud feedback in response to short-term climate variations (circles with error bars); triangles represent the cloud feedback in response to long-term warming [from table 1 of Soden and Held (*3*)]. (**B**) Comparison of the long-wave component of the cloud feedback in response to short-term climate variations. (**C**) Comparison of the short-wave component of the cloud feedback in response to short-term climate variations.

Figure 2B shows a scatter plot of ΔR_{cloud} versus ΔT_s from 100 years of a control run of the ECHAM/MPI-OM climate model, obtained using exactly the same method as was used to analyze the observations. The cloud feedback in the model in response to short-term climate variations is 0.74 ± 0.20 W/m^2/K, which is in reasonable agreement with the observations. r^2 for the fit is about 4%, showing that the models also reproduce the relatively weak control exerted by ΔT_s on ΔR_{cloud}. Table 1 lists the cloud feedback in response to short-term climate variations for eight climate models; these values are also plotted in Fig. 3A.

The models' cloud feedbacks range from 0.34 ± 0.20 to 1.11 ± 0.20 W/m^2/K. Thus, the models paint a consistent picture of positive cloud feedbacks in response to short-term climate variations. The observations fall within the range of models, and taken as a group, there is substantial agreement between the observations and the models' cloud feedback. However, given the large uncertainties, the observations are currently of no obvious help in determining which models most accurately simulate the cloud feedback.

Table 1 and Fig. 3A also show the cloud feedback in response to long-term (centennial-scale) climate change, and there is no correlation between the short-term and long-term cloud feedbacks. This means that even if some models could be excluded on the basis of their short-term climate feedback, it would not necessarily get us any closer to reducing the range of equilibrium climate sensitivity because of the apparent time-scale dependence of the cloud feedback. It should be noted that, because of correlations between the feedbacks (*32*), this analysis does not preclude the possibility that short-term radiative damping rates might still correlate with equilibrium climate sensitivity (*33*).

The long- and short-wave components of the cloud feedbacks are also listed in Table 1 and plotted in Fig. 3, B and C. The observations show that 60 to 80% of the total cloud feedback comes from a positive long-wave feedback, with the rest coming from a weaker and highly uncertain positive short-wave feedback. With the exception of one model, the models also produce positive long-wave cloud feedbacks, a result also in accord with simple theoretical arguments (*34*).

The sign of the short-wave feedback shows more variation among models; it is positive in five of the models and negative in three. There is also a clear tendency for models to compensate for the strength of one feedback with weakness in another. The models with the strongest short-wave feedbacks tend to have the weakest long-wave feedbacks, whereas models with the weakest short-wave feedbacks have the strongest long-wave feedbacks.

Finally, both observations and models have smaller uncertainties in the long-wave feedback than in the short-wave feedback. This means that the long-wave component of ΔR_{cloud} correlates more closely with ΔT_s than the short-wave component.

For the problem of long-term climate change, what we really want to determine is the cloud feedback in response to long-term climate change. Unfortunately, it may be decades before a direct measurement is possible. In the meantime, observing shorter-term climate variations and comparing those observations to climate models may be the best we can do. This is what I have done in this paper. My analysis suggests that the short-term cloud feedback is likely positive and that climate models as a group are doing a reasonable job of simulating this feedback, providing some indication that models successfully simulate the response of clouds to climate variations. However, owing to the apparent time-scale dependence of the cloud feedback and the uncertainty in the observed short-term cloud feedback, we cannot use this analysis to reduce the present range of equilibrium climate sensitivity of 2.0 to 4.5 K.

References and Notes

1. D. A. Randall *et al.*, in *Climate Change 2007: The Physical Science Basis. Contributions of Working Group I to the Fourth Assessment Report of the Intergovernmental Panel on Climate Change*, S. Solomon *et al.*, Eds. (Cambridge Univ. Press, Cambridge, 2007).
2. G. L. Stephens, *J. Clim.* **18**, 237 (2005).
3. B. J. Soden, I. M. Held, *J. Clim.* **19**, 3354 (2006).
4. R. Colman, *Clim. Dyn.* **20**, 865 (2003).
5. M. J. Webb *et al.*, *Clim. Dyn.* **27**, 17 (2006).
6. J. L. Dufresne, S. Bony, *J. Clim.* **21**, 5135 (2008).
7. R. W. Spencer, W. D. Braswell, J. R. Christy, J. Hnilo, *Geophys. Res. Lett.* **34**, L15707 (2007).
8. R. S. Lindzen, Y. S. Choi, *Geophys. Res. Lett.* **36**, L16705 (2009).
9. A. C. Clement, R. Burgman, J. R. Norris, *Science* **325**, 460 (2009).
10. J. D. Neelin *et al.*, *J. Geophys. Res.* **103**, 14261 (1998).
11. A. E. Dessler, S. Wong, *J. Clim.* **22**, 6404 (2009).

12. A. E. Dessler, P. Yang, Z. Zhang, *Geophys. Res. Lett.* **35**, L20704 (2008).
13. B. A. Wielicki *et al.*, *Bull. Am. Meteorol. Assoc.* **77**, 853 (1996).
14. The data used here are the SSF Edition 2.5 1° × 1° gridded, monthly averaged data. Edition 2.5 contains new Edition 3 calibration combined with Edition 2 algorithms and is available from http://ceres.larc.nasa.gov.
15. N. G. Loeb *et al.*, *J. Clim.* **20**, 575 (2007).
16. B. J. Soden *et al.*, *J. Clim.* **21**, 3504 (2008).
17. K. M. Shell, J. T. Kiehl, C. A. Shields, *J. Clim.* **21**, 2269 (2008).
18. A. Simmons, S. Uppala, D. Dee, S. Kobayashi, ERA-Interim: New ECMWF reanalysis products from 1989 onward (*ECMWF Newsletter* **110**, Winter 2006/2007). Data can be downloaded from www.ecmwf.int/products/data.
19. M. J. Suarez *et al.*, The GEOS-5 Data Assimilation System—documentation of versions 5.0.1, 5.1.0, and 5.2.0, NASA/TM–2008–104606, Vol. 27, 2008. Data can be downloaded from http://disc.sci.gsfc.nasa.gov.
20. A. E. Dessler *et al.*, *J. Geophys. Res.* **113**, D17102 (2008).
21. L. Moy *et al.*, *J. Geophys. Res.* **115**, D15110 (2010).
22. B. J. Sohn, R. Bennartz, *J. Geophys. Res.* **113**, D20107 (2008).
23. C. A. Smith, P. D. Sardeshmukh, *Int. J. Climatol.* **20**, 1543 (2000).
24. K. E. Trenberth, J. T. Fasullo, C. O'Dell, T. Wong, *Geophys. Res. Lett.* **37**, L03702 (2010).
25. D. M. Murphy, *Geophys. Res. Lett.* **37**, L09704 (2010).
26. M. H. Zhang, J. J. Hack, J. T. Kiehl, R. D. Cess, *J. Geophys. Res.* **99**, 5525 (1994).
27. R. W. Spencer, W. D. Braswell, *J. Geophys. Res.* **115**, D16109 (2010).
28. I. M. Held, B. J. Soden, *Annu. Rev. Energy Environ.* **25**, 441 (2000).
29. K. Minschwaner, A. E. Dessler, *J. Clim.* **17**, 1272 (2004).
30. A. E. Dessler, S. C. Sherwood, *Science* **323**, 1020 (2009).
31. G. A. Meehl *et al.*, *Bull. Am. Meterol. Soc.* **88**, 1383 (2007).
32. P. Huybers, *J. Clim.* **23**, 3009 (2010).
33. E. S. Chung, B. J. Soden, B. J. Sohn, *Geophys. Res. Lett.* **37**, L10703 (2010).
34. M. Zelinka, D. L. Hartmann, *J. Geophys. Res.* **115**, D16117 (2010).
35. I thank the CERES, MERRA, and ECMWF groups for producing the data used in this paper. Support for this work came from NASA grant NNX08AR27G to Texas A&M University. I also acknowledge useful contributions from N. Loeb, M. Bosilovich, J.-J. Morcrette, M. Zelinka, P. Stackhouse, T. Wong, J. Fasullo, P. Yang, and G. North. Finally, I acknowledge the modeling groups, the Program for Climate Model Diagnosis and Intercomparison, and the WCRP's Working Group on Coupled Modeling for their roles in making available the WCRP CMIP3 multimodel data set. Support of this data set is provided by the U.S. Department of Energy Office of Science.

19 May 2010; accepted 9 November 2010
10.1126/science.1192546

Stochastic Late Accretion to Earth, the Moon, and Mars

William F. Bottke,[1]* Richard J. Walker,[2] James M. D. Day,[2,3] David Nesvorny,[1] Linda Elkins-Tanton[4]

Core formation should have stripped the terrestrial, lunar, and martian mantles of highly siderophile elements (HSEs). Instead, each world has disparate, yet elevated HSE abundances. Late accretion may offer a solution, provided that ≥0.5% Earth masses of broadly chondritic planetesimals reach Earth's mantle and that ~10 and ~1200 times less mass goes to Mars and the Moon, respectively. We show that leftover planetesimal populations dominated by massive projectiles can explain these additions, with our inferred size distribution matching those derived from the inner asteroid belt, ancient martian impact basins, and planetary accretion models. The largest late terrestrial impactors, at 2500 to 3000 kilometers in diameter, potentially modified Earth's obliquity by ~10°, whereas those for the Moon, at ~250 to 300 kilometers, may have delivered water to its mantle.

Highly siderophile elements (HSEs: Re, Os, Ir, Ru, Pt, Rh, Pd, Au) have low-pressure metal-silicate partition coefficients that are extremely high (>10^4) (*1*). Hence, a common assumption has been that the silicate portions of rocky planetary bodies with metallic cores are effectively stripped of HSEs immediately after primary accretion and final core segregation (*2*). Accordingly, the "giant impact" on Earth that formed the Moon 60^{+90}_{-10} million years (My) after formation of the earliest solids should have cleansed HSEs from the mantles of both worlds (*3*–*5*).

However, studies of mantle-derived terrestrial peridotites (olivine-rich rocks that dominate Earth's upper mantle) have shown that, not only are HSE abundances in Earth's mantle much higher than expected (at ~0.008 × CI-chondrite meteorites), but their HSE proportions are also approximately the same as chondritic meteorites (Fig. 1) (*6*). Although we have no direct samples of martian or lunar mantle rocks, studies of HSE and Os isotopes in derivative mantle melts suggest roughly equivalent absolute abundances in the martian mantle (*7*, *8*), but much lower abundances in the lunar mantle (≤0.0004 × CI-chondrite) (*9*–*11*), with HSEs in chondritic relative proportions for both bodies (Fig. 1) (*7*, *10*).

Although different scenarios have been proposed to produce the relatively high absolute and chondritic relative abundances of HSEs in planetary mantles (*12*), perhaps the most straightforward process is delivery from continued planetesimal accretion after the last core-formation event, with the materials mixed into the mantle by convection (*13*). Such events would represent a natural continuum from a planet-formation perspective, with the Mars-sized projectile that produced the giant impact representing the largest component of the leftover planetesimal population that continued to bombard the planets until surviving projectiles were depleted by collisional and dynamical processes (*14*).

We used the estimated collective distribution of HSEs in the terrestrial, martian, and lunar mantles to test whether their abundances were set by late accretion. For Earth, late accretion of ~2.0×10^{22} kg of material with bulk chondritic

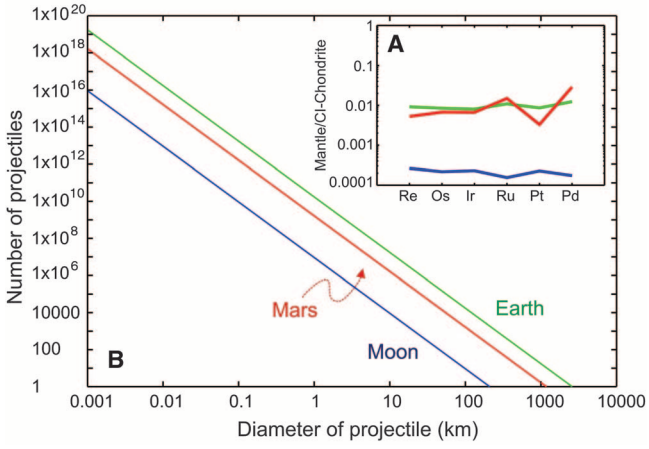

Fig. 1. (**A**) Estimated martian and lunar mantle HSE abundances and patterns versus terrestrial orogenic peridotites and relative to CI-chondrites. Earth, Mars, and the Moon are shown in green, red, and blue, respectively. Estimates for mantle compositions were made by regressing Os, Ir, Ru, Pt, Pd, and Re versus MgO data (*10*). The flat patterns indicate that all three mantles have approximately chondritic relative abundances of the HSEs, although the Moon's mantle abundances are >20 times less than those of Earth. (**B**) Minimum number and sizes of late accretion chondritic projectiles needed to deliver the estimated abundances of HSEs to the mantles of the Moon, Mars, and Earth, assuming 100% accretion efficiency. These values are lower limits in terms of delivered mass because the process is unlikely to be 100% efficient.

[1]Southwest Research Institute and NASA Lunar Science Institute, 1050 Walnut Street, Suite 400, Boulder, CO 80302, USA. [2]Department of Geology, University of Maryland, College Park, MD 20742, USA. [3]Geosciences Research Division, Scripps Institution of Oceanography, La Jolla, CA 92093, USA. [4]Massachusetts Institute of Technology, Cambridge, MA 02139, USA.

*To whom correspondence should be addressed. E-mail: bottke@boulder.swri.edu